In Übereinstimmung mit diesem Befund ist die Tatsache, dass $Ba_{15}Fe_7S_{25}$ (Fe mit der formalen Oxidationszahl + 2·86) nicht in einer Ba_3SiS_5-Variante, sondern in einer $(NH_4)_3ZnCl_5$-Variante kristallisiert.

Literatur

BÄRNIGHAUSEN, H. (1974). Privatmitteilung.

BÄRNIGHAUSEN, H., KLEE, W. E. & WONDRATSCHEK, H. (1975). *Symmetriebeziehungen zwischen verwandten Kristallstrukturen: Anwendungen der kristallographischen Gruppentheorie in der Kristallchemie.* An der Univ. Karlsruhe veranstalteter Kurs (unveröffentlichtes Manuskript).

BILTZ, W. (1934). *Raumchemie der festen Stoffe.* Leipzig: Voss-Verlag.

CLEGG, W., BROWN, M. L. & WILSON, L. J. A. (1976). *Acta Cryst.* B**32**, 2905–2906.

CROMER, D. T. & WABER, J. T. (1974). In *International Tables for X-ray Crystallography*, Bd. IV. Birmingham: Kynoch Press.

DENT GLASSER, L. S. & GLASSER, F. P. (1965). *Acta Cryst.* **18**, 453–454.

HOPPE, R. (1966). *Angew. Chem. Int. Ed. Engl.* **5**, 52–63.

HOPPE, R. (1970). *Adv. Fluorine Chem.* **6**, 387–438.

HOPPE, R. & MEHLHORN, B. (1976). *Z. Anorg. Allg. Chem.* **425**, 200–208.

International Tables for X-ray Crystallography (1952). Bd. I. Birmingham: Kynoch Press.

JAULMES, P. (1974). *Acta Cryst.* B**30**, 2283–2285.

JEITSCHKO, W. & DONOHUE, P. C. (1975). *Acta Cryst.* B**31**, 1890–1895.

KAPUSTINSKI, A. (1933). *Z. Phys. Chem. Abt. B*, **22**, 257–260.

KLUG, H. P. & ALEXANDER, L. (1944). *J. Am. Chem. Soc.* **66**, 1056.

LEMLEY, J. T., JENKS, I. M., HOGGINS, I. T., ELIEZER, Z. & STEINFINK, H. (1976). *J. Solid State Chem.* **16**, 117–128.

MARTÍNEZ-RIPOLL, M. & BRAUER, G. (1974). *Acta Cryst.* B**30**, 1083–1087.

MEERBURG, P. A. (1903). *Z. Anorg. Chem.* **37**, 199–221.

PAULING, L. (1929). *J. Am. Chem. Soc.* **51**, 1010–1021.

PEARSON, W. B. (1972). In *The Crystal Chemistry and Physics of Metals and Alloys.* New York: John Wiley.

POWELL, H. M. & WELLS, A. F. (1935). *J. Chem. Soc.* S. 359–362.

SEIFERT, H.-J. & STÄUDEL, L. (1978). *J. Solid State Chem.* **26**, 397–399.

SHANNON, R. D. (1976). *Acta Cryst.* B**32**, 751–767.

WANG, Y., GABE, E. J., CALVERT, L. D. & TAYLOR, J. B. (1976). *Acta Cryst.* B**32**, 1440–1445.

Acta Cryst. (1981). B**37**, 525–532

Charge Density in Anhydrite, $CaSO_4$. II. Static Deformation Density Distributions from a Multipole Refinement

BY A. KIRFEL AND G. WILL

Mineralogisches Institut der Universität Bonn, Lehrstuhl für Kristallographie und Mineralogie, Poppelsdorfer Schloss, D-3500 Bonn, Federal Republic of Germany

(*Received* 18 *August* 1980; *accepted* 1 *October* 1980)

Abstract

Two multipole-expansion refinements have been performed on X-ray data up to $s = 1{\cdot}078$ Å^{-1} obtained from a natural anhydrite specimen. In the first refinement ($R_w = 0{\cdot}0116$) the standard crystallographic parameters have been varied along with the multipole coefficients leading to a static (X–X) deformation density distribution. The second refinement ($R_w = 0{\cdot}0138$) has been performed with fixed positional and thermal parameters from neutron diffraction data up to $s = 1{\cdot}01$ Å^{-1}. The resultant multipole expansion can be regarded as describing a static (X–N) deformation density distribution. Both expansions are compared with our previous dynamic (X–X) and (X–N) deformation densities. The interesting sections are discussed in terms of the information concerning bond-induced charge redistributions in the electron shells. With crystal neutrality imposed, a charge analysis of both refinements confirms the Ca cation to be twofold positive, and hence the anion to be $[SO_4]^{2-}$. The observation of a dipole moment of the anion is discussed.

Introduction

In a previous paper (Kirfel & Will, 1980*a*), hereafter referred to as part I, we described X-ray and neutron

0567-7408/81/030525-08$01.00

diffraction measurements on natural anhydrite, $CaSO_4$, from Stassfurt, Federal Republic of Germany. Various refinements of the data were presented, and we discussed the results in terms of standard crystallographic parameters as well as dynamic deformation density distributions, $(X-X)$ and $(X-N)$. The important result of these investigations was the deviation of the deformation density associated with the $[SO_4]^{2-}$ anion from earlier findings obtained from comparable atomic arrangements. Instead of clearly recognizable σ-bond charge accumulations along S–O due to sp^3 hybridization of the sulfur valence electrons, we found a much more delocalized electron distribution, which may be interpreted qualitatively by a considerable degree of $3d$ population of the S electron shell. Outside the $[SO_4]^{2-}$ complex we observed additional charge accumulations lying on the connecting lines of the Ca and O atoms, which can be associated with O lone-pair electrons. In the course of the above refinements we also performed two multipole-expansion refinements of the X-ray data to check for a significant improvement of the analytical model describing the observed electron density. Thus, we aimed to investigate to what extent the multipole-expansion method is capable of dealing with the above-mentioned more delocalized electron distribution, and to establish static deformation density distributions in the interesting sections of the unit cell. In the present paper we discuss the results of ensuing investigations on the bond density in anhydrite.

Multipole-expansion refinements

A good many of the multipole-expansion refinements have been described in part I. Therefore, here we summarize briefly the main points. Two multipole-expansion refinements were performed with the X-ray data with *LS-EXP* (Hirshfeld, 1971; Harel & Hirshfeld, 1975). In this treatment the charge density for each atom j is expressed as a superposition of a spherical free-atom density ρ_j^{at} plus a deformation density $d\rho_j$ that is approximated by a linear combination of localized atomic deformation functions. Thus, each atomic density is composed of the free-atom density and an expansion in the associated multipoles ψ_{jl} centered at the particular atom position:

$$\rho_j = \rho_j^{at} + \sum_l \psi_{jl} c_{jl}.$$

This atomic position, if refinable, is of course model dependent. Each set of multipole functions which describes the deviations of the charge density from free-atom spherical symmetry induced by bonding has to be specified with respect to an atomic coordinate system. This system is defined by allocating a first- and second-neighbor atom, the direction towards the first giving the L axis, the M axis being in the plane of the three atoms, and the N axis perpendicular to that plane. The coordinate system in the present case is given in Table 1, and Fig. 1 shows the positions and orientations of the individual atomic systems. The refinement was carried out by two strategies labelled MULT1 and MULT2. MULT1 was conventional in the sense that the standard crystallographic parameters were allowed to vary along with the deformation-function coefficients and the α coefficients, although in alternating cycles. For MULT2 the standard parameters were taken from the neutron diffraction experiment (part I) as being the true ones, which means unbiased by bonding. With these parameters fixed, the multipole expansion was thus forced to adjust to a static $(X-N)$ density distribution. Therefore, the two refinements differ. In the first the multipole origins are fixed to the centers of gravity of the individual atomic electron shells to be adjusted by variation of the positional parameters. In the second the multipoles are

Table 1. *Refined α values and multipole coefficients $c_{jl} > 3\,\sigma(c_{jl})$*

$A = \sqrt{2} - 1.$

	MULT1	MULT2
α(Ca)	7·0	9·0
α(S)	10·3	7·1
α(O)	5·1	6·5

	First neighbor	Second neighbor	Order	Direction	MULT1 c_{jl}	MULT2 c_{jl}
Ca	S	O(1)	0		0·26	0·21
			4	1A1	−0·47	
S	Ca	O(1)	0		−0·19	
			1	100	−0·33	
			2	110	0·43	0·59
			4	010		−0·89
			4	A11	−0·45	
			4	1A1	−0·41	−1·12
O(1)	S	Ca	0		−0·23	−0·26
			1	100	0·30	
			1	010	−0·43	
			2	110	0·49	
			2	1$\bar{1}$0	0·52	
			2	101	0·52	
			3	110	1·02	1·33
			3	1$\bar{1}$0		0·89
			3	101		0·95
			3	111		−1·10
			3	1$\bar{1}\bar{1}$		−0·87
			4	100	0·77	
			4	1$\bar{A}$1	−0·55	
			4	$A\bar{1}$1	−0·92	
O(2)	S	Ca	1	100		−0·25
			3	110	1·31	0·92
			3	1$\bar{1}$0	1·04	1·09
			3	101	1·28	1·01
			3	111	−1·31	−0·90
			3	1$\bar{1}\bar{1}$	−1·21	−1·09
			4	100	1·11	0·99

fixed to the atomic nuclei. Similarly, the set of multipoles was treated as performing the harmonic vibrations of the spherical electron shells in the first case, and as vibrating as the nuclei in the second. Therefore we have to distinguish between a refined $d\rho$ describing (to whatever degree) that part of the observed density which is not accessible by the conventional spherical-atom model (with all possible correlation problems encountered), and a $d\rho$ describing the residual density $(X–N)$, both based on the convolution approximation, which assumes that the vibrational modes of the outer valence electrons correspond to those of the closed electron shells or the nuclei respectively. With this distinction we should not be surprised when we find different deformation density distributions when the bonding involves polarization of individual atoms. In this case differences can also be expected between numerical results derived from the analytical descriptions of both deformation densities, such as formal charges or dipole moments.

As already outlined in part I, the set of multipole functions (up to order 4) comprised 110 non-vanishing members, of which 64 were independently adjustable due to the atomic site symmetries *mm* for Ca and S, and *m* for both O atoms. All multipole coefficients were zero at the beginning of the refinements. The α coefficients describing the radial dependency of the multipoles were initially set to $\alpha(S) = 12{\cdot}0$, $\alpha(O) = 8{\cdot}0$ and $\alpha(Ca) = 10{\cdot}0$. The refinement was carried out in alternating cycles for the 21 standard parameters, the 64 multipole coefficients, and the 3 α's. For MULT2 there was only one standard parameter, the scale factor. At the beginning, strongly damped parameter shifts were found to be useful to guarantee a steady development of the multipoles. The dampening was gradually diminished when the multipole coefficients approached their final values. Fig. 2 shows as an example the monitor curves of four coefficients. Stable values of the c_{jl} were reached after 67 cycles for both cases, and the final R values are (values in parentheses with unobserveds omitted): MULT1: $R_{overall} = 0{\cdot}0280$ $(0{\cdot}0156)$ and $R_W = 0{\cdot}0147$ $(0{\cdot}0116)$; MULT2: $R_{overall} = 0{\cdot}0310$ $(0{\cdot}0185)$ and $R_w = 0{\cdot}0165$ $(0{\cdot}0138)$.

In a Hamilton test all R(MULT1)/R(MULT2) ratios show that MULT1 corresponds to a significant model improvement compared to MULT2, well below the 0·005 confidence level. The same result is obtained when we compare MULT1 and MULT2 with the refinements of part I. Only the bond model (BM) represents a better approach to the observed density than MULT2.

Table 1 shows the final α values and the multipole coefficients $c_{jl} > 3\sigma$, which dominate the static deformation density expansions in both models. The refined standard crystallographic parameters obtained from MULT1 as well as those from the neutron experiment used for MULT2 have been given in Tables 4 and 5 of part I. Significant differences in the positional parameters were observed only for S and O(1), implying that the two considered deformation density expansions associated with these atoms could develop differently, whereas those associated with Ca and O(2) could be expected to behave similarly. A survey of the coefficients of Table 1 supports this numerically.

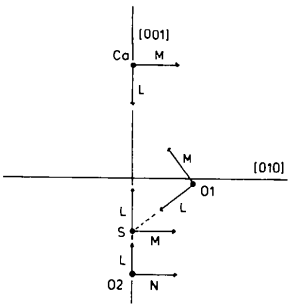

Fig. 1. Positions and orientations of the individual atomic coordinate systems (axes L, M, N) viewed along [100].

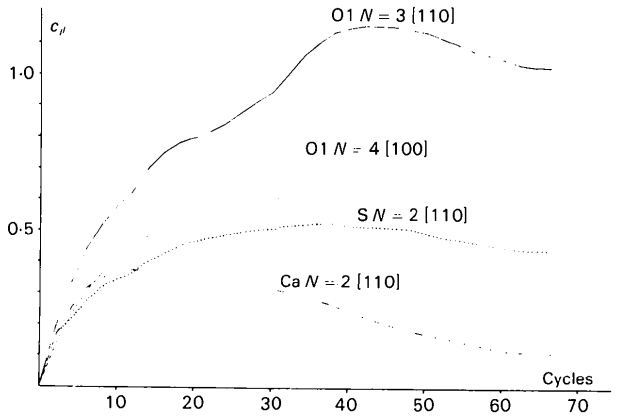

Fig. 2. Monitor curves of selected multipole coefficients c_{jl}.

Static deformation densities

The analytical form of the deformation density expansion $d\rho$ can be employed for two-dimensional sections of any required orientation. Fig. 3(*a*) and (*b*) shows the resultant $(X–X)$ static deformation density distributions in the two mirror planes perpendicular to each other and containing the angles O(1)–S–O(1) and O(2)–S–O(2) respectively. The corresponding $(X–N)$ static deformation densities are depicted in Fig. 4(*a*) and (*b*). For clarity it should be noted here that all O(2)–S–O(2) sections are in reversed orientation, *e.g.* the S···Ca direction is parallel to $[00\bar{1}]$. Using the e.s.d.'s of the refined multipole coefficients along with the correlation matrix we have also calculated the corresponding error maps $\sigma(d\rho)$. σ is generally large at

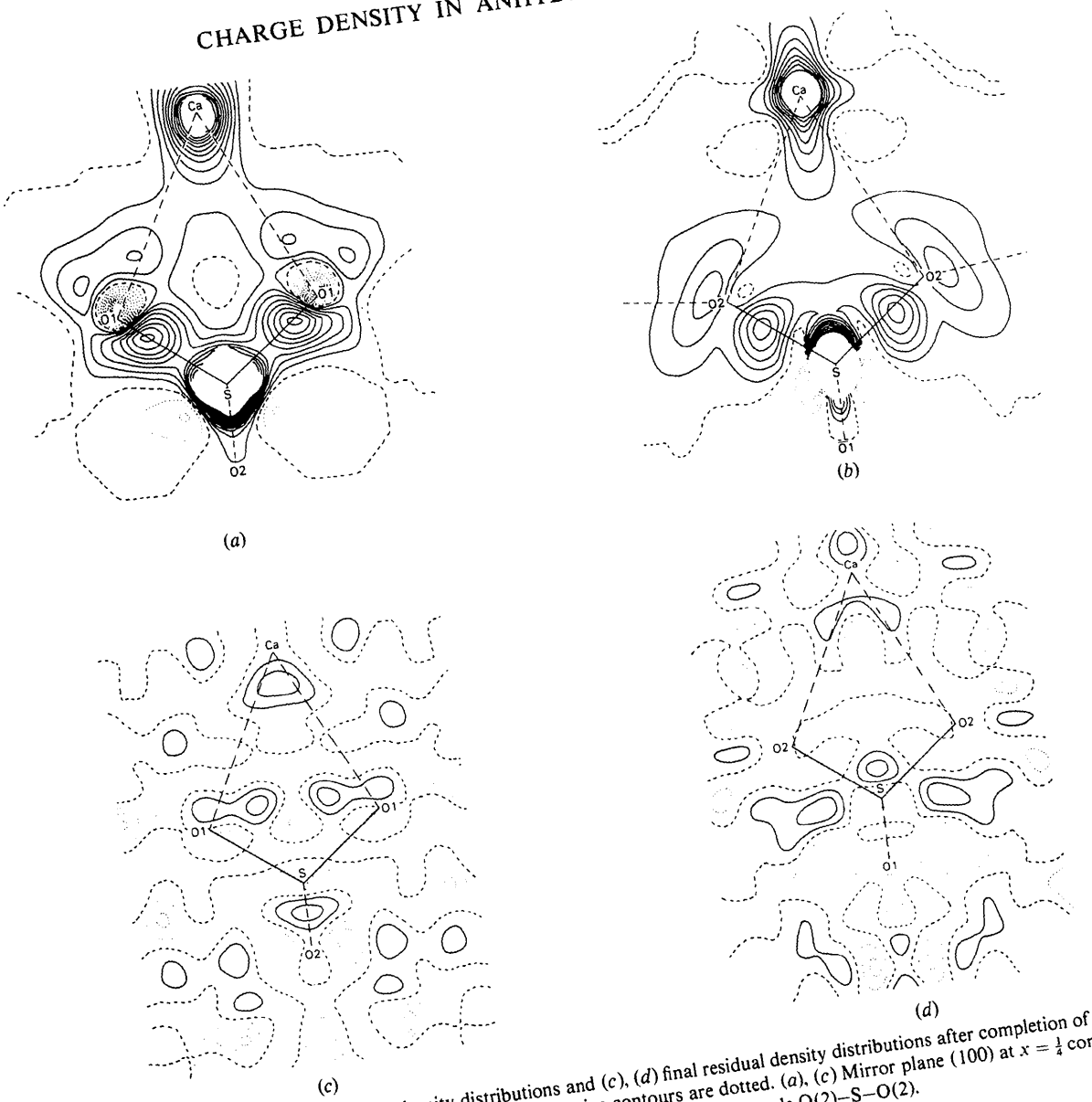

Fig. 3. (*a*), (*b*) Static (*X*–*X*) deformation density distributions and (*c*), (*d*) final residual density distributions after completion of refinement MULT1. Levels are at 0·1 e Å^{-3}, the zero line is broken, negative contours are dotted. (*a*), (*c*) Mirror plane (100) at $x = \frac{1}{4}$ containing the bond angle O(1)–S–O(1); (*b*), (*d*) mirror plane (010) at $y = 0$ containing the bond angle O(2)–S–O(2).

the atomic positions, and the blank areas around the atomic centers in Figs. 3 and 4 correspond to $\sigma(d\rho) >$ 0·2 e Å^{-3}.

The quality of the $d\rho$ expansion can be estimated from a comparison of the MULT2 sections (Fig. 4*a*,*b*) with Figs. 2(*c*) and 3(*c*) of part I. In both cases the maps are based on the crystallographic standard parameters from the neutron measurements. Hence, Fig. 4(*a*), (*b*) represents the analytical description of the (*X*–*N*) residual density of part I, but deconvoluted with respect to the nuclear vibrations. Considering the positions and heights of the individual charge accumulations of the S–O and O···Ca bonds, the qualitative agreement between the comparable sections is satisfactory, although the features of the MULT2 sections are more pronounced. This is especially true for the peaks on the O···Ca connecting lines (*cf.* Table 2), and for the redistribution of charge density in the S electron shell. Looking along the bisectors of the O–S–O bond angles we find that in both sections the static (*X*–*N*) deformation density expansion reproduced neither the residual density peak in the middle of O(2)–S–O(2) (Fig. 2*c*, part I) nor the positive density band in O(1)–S–O(1) (Fig. 3*c*, part I). There remain, however, significant and distinct density accumulations on the O–S–O bisectors. This observation is in contrast to comparable results obtained from $Na_2S_2O_6.2H_2O$ (Kirfel & Will, 1980*b*), and supports the existence of a significant 3*d*-orbital population in the S electron shell in $CaSO_4$.

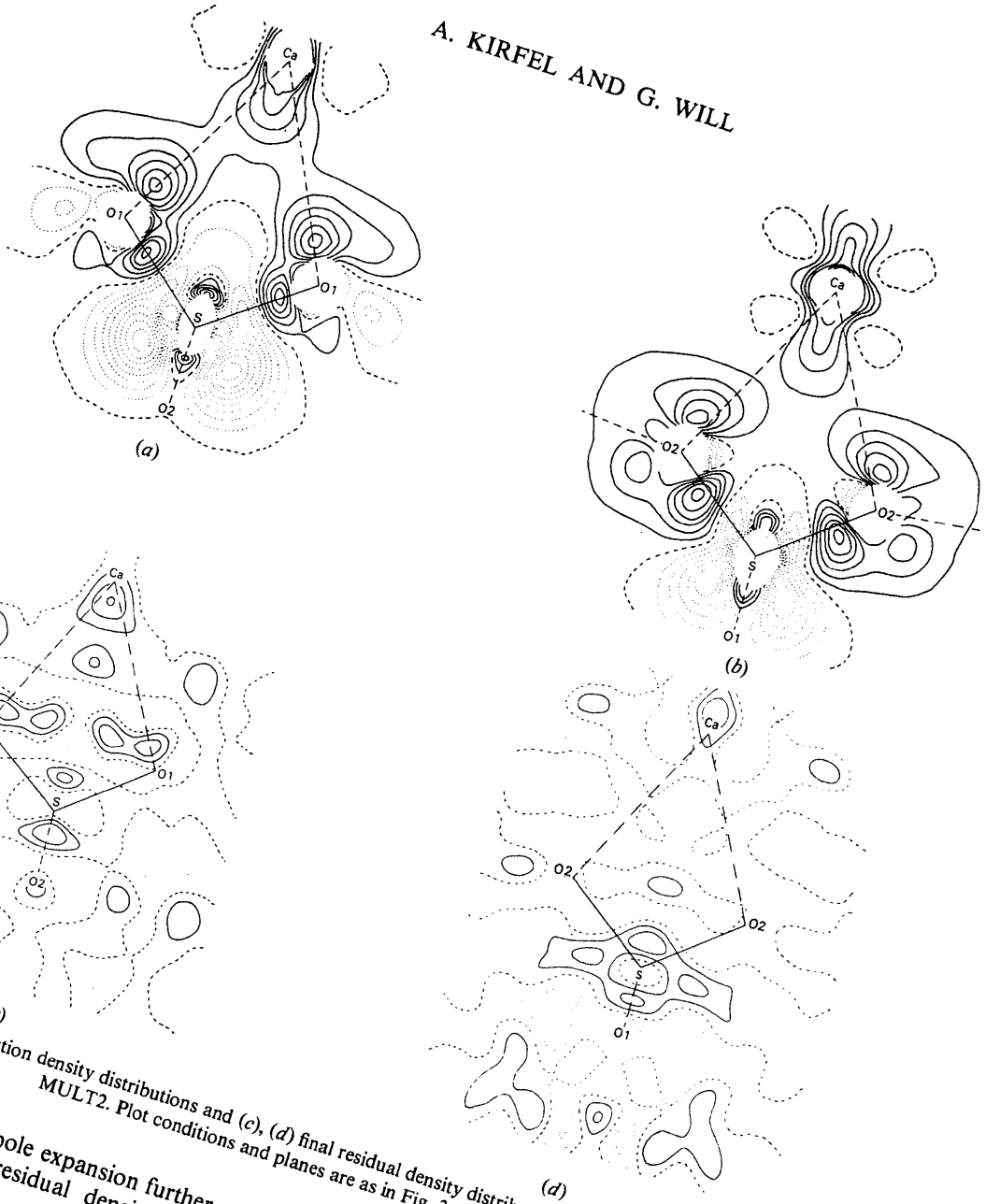

Fig. 4. (*a*), (*b*) Static (*X*–*N*) deformation density distributions and (*c*), (*d*) final residual density distributions after completion of refinement MULT2. Plot conditions and planes are as in Fig. 3.

To analyze the fit of the multipole expansion further we have also calculated final residual density distributions:

$$\Delta\rho = \frac{1}{K}\rho_{obs} - \rho_{calc}^{MULT2},$$

which are depicted in Fig. 4(*c*) and (*d*). Significant features in these maps serve to show whether there is observed density which is not assessed by the model. From Fig. 4(*c*), (*d*) we observe that the (*X*–*N*) density sociated with the S–O bonds is described properly. e same applies for the density distribution around). The only interesting residual density ac- ulations of the order of 0·2 eÅ^{-3} are again on or to the bisectors of the O–S–O bond angles, giving once more experimental evidence of a 3*d*–2*p* interaction between the S and O atoms.

How does the picture change when we proceed to the results of the pure *X*-ray static deformation density of

Table 2. *Peak heights* (e Å^{-3}) *on the* S–O *bonds and along* O···Ca

	MULT1	MULT2	(*X*–*N*)*	(*X*–*X*)*	NAH/D†
S–O(1)	0·8	0·5	0·4	0·5	
S–O(2)	0·5	0·6	0·5	0·5	
O(1)···Ca	0·3	0·6	0·3	0·5	0·5
O(2)···Ca	0·3	0·5	0·3	0·4	
				0·2	

* Part I (Kirfel & Will, 1980*a*).
† Average S–O σ-bond peak height from $Na_2S_2O_6.2(H/D)_2O$ (Kirfel & Will, 1980*b*).

MULT1 (Fig. 3*a* and *b*), which has yielded by far the best agreement factor? The general appearance within the $[SO_4]^{2-}$ ion has not changed much as far as the charge accumulations associated with the σ bonds are concerned. However, they seem to be better developed, and this multipole expansion partially reproduces the positive density distribution connecting the σ-bond peaks inside the O–S–O bond angles, as observed in part I. This can only be due to the allowed variation of the positional and vibrational parameters of the atoms, from which we can conclude (in agreement with part I) that the centers of gravity of the deformed electron clouds do not coincide with the nuclear positions, *i.e.* we observe a polarization. The same argument holds for the charge accumulations outside SO_4. Compared to those of Fig. 4(*a*),(*b*) they are lower and broader, implying that the O–Ca interaction is smaller than indicated by the MULT2 results. As for MULT2, we find some residual peaks of the order of 0·2 e Å^{-3} in the final residual density maps calculated after the completion of MULT1 (Fig. 3*c* and *d*). These peaks are again on or close to the O–S–O bisectors, and for the section O(2)–S–O(2) exactly on that crosspoint of imaginary lines connecting Ca^{I}–O(2) and Ca^{II}–S, as reported in part I. This finding not only corroborates these earlier results but also shows that the model MULT1 was not able to deal completely with the more delocalized valence-electron distribution in $[SO_4]^{2-}$ of anhydrite.

The individual linear combinations of atomic deformation functions were used in *LS-EXP* to calculate formal atomic charges and dipole moments with respect to the coordinate system of Fig. 1. The results are listed in Table 3. Such straightforward calculations are not based on molecular-partitioning schemes, and the differences in the charge values of Table 3 demonstrate the difficulties encountered in such simple calculations. The charges come from that part of the

Table 3. *Formal charges* (e) *and dipole-moment components D* (eÅ) *from the refinements MULT*1 (*X–X, upper row*) *and MULT*2 (*X–N, lower row*)

Values resulting from weighted averaging are given in parentheses.

	Charge	$D(L)$	$D(M)$
Ca^{2+}	0·09	−0·01	
	0·06	0·01	
	(0·065)	(0·00)	
S	1·33	0·03	
	4·40	−0·03	
	(2·43)	(0·03)	
O(1)	0·04	−0·10	0·69
	−1·24	0·44	0·20
	(−0·71)	(0·21)	(0·38)
O(2)	−1·75	0·44	−0·06
	−1·99	0·38	−0·16
	(−1·83)	(0·40)	(−0·11)

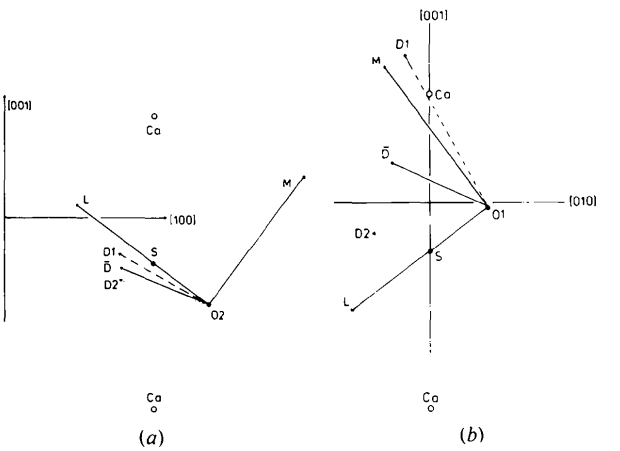

Fig. 5. Schematic drawing of O atom dipole moments from refinements MULT1 (*D*1), MULT2 (*D*2), and weighted averaging. (*a*) Mirror plane (010) at $y = 0$ containing O(2)–S–O(2); (*b*) mirror plane (100) at $x = \frac{1}{4}$ containing O(1)–S–O(1).

observed density which is not accounted for by the underlying conventional spherical-atom model; in other words, the degree of separation of thermal smearing and bond-induced charge redistribution determines the numerical results obtained from the integrations of refined multipole-function sets. Since the adjustment of temperature tensors (symmetry *mmm*), as in MULT1, can yield too large vibrational parameters, $d\rho$ can become too small on average with the result that the charges may be underestimated. *Vice versa*, from the neutron measurements temperature tensors may be too small (most likely due to a lack of thermal-diffuse-scattering correction), leading to larger values of $d\rho$, resulting in overestimated charges. Both tendencies seem to influence the present investigation. Nevertheless, two common results can be extracted from Table 2: (*a*) the Ca^{2+} ion is twofold positive yielding a truly twofold negative anion $[SO_4]^{2-}$ since only neutrality of the crystal has been imposed; (*b*) O(2) is more negatively charged than O(1).

Considering the dipole moments exerted by the individual atomic charge distributions, we find no indications for dipolar distributions on Ca^{2+} and S, but we do find dipoles associated with the O atoms. Similar to their charge values, the dipoles found for O(2) from MULT1 and MULT2 are almost in agreement (Fig. 5*a*). The dipole vector of the O(2) electron shell is pointing towards the S atom, however, with a component towards the center of the triangle O(2)–S–O(2). A severe difference is found for O(1), which according to MULT1 shows a considerable dipole moment directed towards Ca^{2+} (Fig. 5*b*). From MULT2 we find for O(1) about the same polarization as for O(2), both magnitudes and orientations with respect to the O–S–O bond angles being approximately equal. The resultant dipole moment of the $[SO_4]^{2-}$ anion is

therefore practically vanishing when considering the results of MULT2, whereas MULT1 yields a dipole pointing along [001] towards Ca^{2+}. The existence of such a dipole moment as indicated by MULT1 is supported by the shorter S–Ca distance along the bisector of O(2)–S–O(2) [3·104 (1) compared to 3·141 (1) Å].

Conclusions

Application of the multipole refinement for the evaluation of static (X–X) and (X–N) deformation density distributions has brought significant model improvements in comparison with the conventional all-data and high-order refinements of part I. The value of analytical descriptions of bond-induced electron-shell deformations is evident for $CaSO_4$. Comparing the two applied models, MULT1, *i.e.* the superposition of a spherical free-atom electron distribution plus an adjustable deformation density, both vibrating with identical adjustable harmonic modes around an adjustable position, is superior to MULT2, in which the spherical electron distribution as well as the adjustable deformation density is forced to vibrate as the nucleus around the position of the latter. This statement is correct in terms of the agreement factors, but is it also correct with respect to the information about the bonding features in $CaSO_4$ which we want to extract from such investigations? Does a straightforward application of the multipole-expansion refinement perhaps hide or suppress information which in its main features may be exaggerated when looking at the static (X–N) deformation density? At present we do not have a satisfactory answer. However, if the question can be answered positively, it would be justified to search for the better representation of bonding effects between the two possibilities, *e.g.* to look at the weighted average of $d\rho$ of both models. Fig. 6(*a*) and (*b*) shows the resultant static deformation density distributions from averaging. The maps repeat the information from Figs. 3 and 4, but in a smoother way, and still express the differences between O(1) and O(2). In Table 3 and Fig. 5(*a*), (*b*) we have also given the formal charges and dipole-moment components resulting from the averaging. According to these values we find formal charges of +2·4 for S, −0·7 for O(1), and −1·8 for O(2). The dipole moment of the $[SO_4]^{2-}$ anion would still point along [001]. All the values of Table 3 have to be considered as indications rather than physical properties since the method of evaluation is doubtful. However, they may serve to express tendencies which should be investigated in more detail.

A view of the main bond-induced charge accumulations associated with the $[SO_4]^{2-}$ anion is depicted in Fig. 7. This deformation density distribution is calculated only with the multipoles of the O

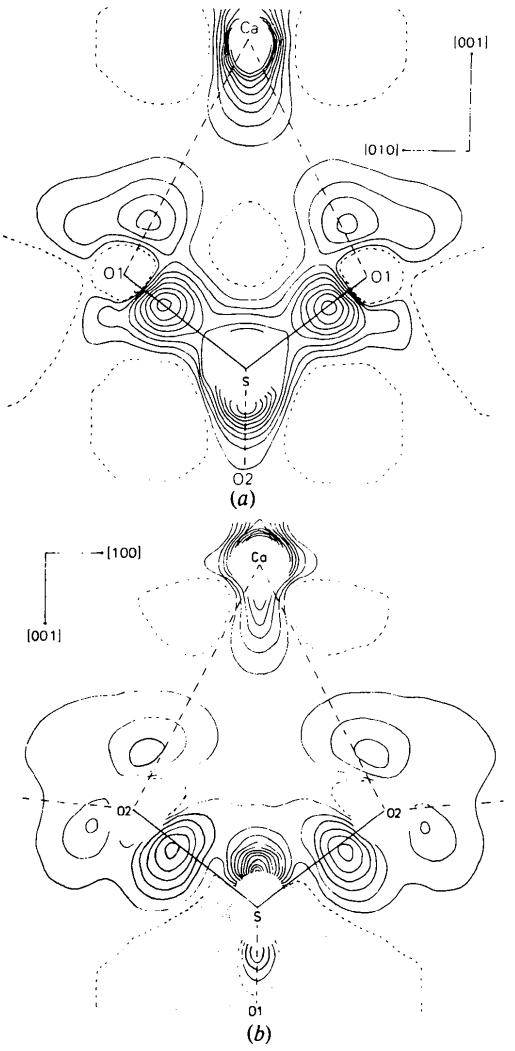

Fig. 6. Static deformation density distributions from weighted average of (X–X) and (X–N) multipole expansions. Levels are at 0·1 e Å^{-3}, the zero line is broken, negative contours are dotted. (*a*) Mirror plane (100) containing O(1)–S–O(1); (*b*) mirror plane (010) containing O(2)–S–O(2).

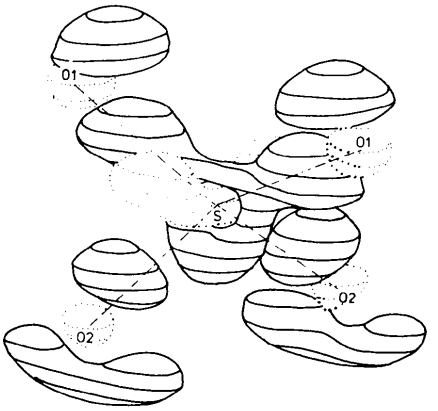

Fig. 7. Three-dimensional envelopes of the positive and negative (dotted) static deformation density at ±0·3 e Å^{-3} calculated from the averaged S and O multipole coefficients from MULT1 and MULT2.

and S atoms after weighted averaging. The method of plotting has been described earlier (Kirfel & Will, 1980*b*). The picture shows the three-dimensional envelopes of the positive and negative static deformation density at $\pm 0{\cdot}3$ e Å^{-3}, from which we can easily recognize the S–O bond-charge accumulations, the positive density within the O–S–O bond angles, and the lone-pair regions of the O atoms outside the SO_4 tetrahedron.

This work has received the support of the Deutsche Forschungsgemeinschaft, which is gratefully acknowledged.

References

HAREL, M. & HIRSHFELD, F. L. (1975). *Acta Cryst.* B**31**, 162–172.
HIRSHFELD, F. L. (1971). *Acta Cryst.* B**27**, 769–781.
KIRFEL, A. & WILL, G. (1980*a*). *Acta Cryst.* B**36**, 2881–2890.
KIRFEL, A. & WILL, G. (1980*b*). *Acta Cryst.* B**36**, 512–523.

Acta Cryst. (1981). B**37**, 532–545

MX_4-Ketten aus kantenverknüpften Oktaedern: mögliche Kettenkonfigurationen und mögliche Kristallstrukturen

VON ULRICH MÜLLER

Fachbereich Chemie der Universität Marburg, Hans-Meerwein-Strasse, D-3550 Marburg, Bundesrepublik Deutschland

(*Eingegangen am* 7. *Juli* 1980; *angenommen am* 9. *Oktober* 1980)

Abstract

Compounds of the composition MX_4 are frequently built up from chains consisting of edge-sharing octahedra. The two terminal (non-bridging) X atoms of an octahedron can have a *cis* or *trans* arrangement; if only one kind of arrangement occurs, the resulting chains are called *cis* or *trans* chains, respectively. The *trans* chain is always linear whereas a *cis* chain can have an infinite variety of configurations. This is because any group of four *cis*-connected octahedra can adopt one of four configuration types, designated by the symbols *e*, *g*, *s* and *z*. The configuration of any *cis* chain can be uniquely characterized by a sequence of these symbols. A symbolism for chains having *cis* and *trans* octahedra is also presented. Under the condition that the packing of chains is performed in a way such that the X atoms form a close-packing arrangement, certain chain types cannot be realized, and of the rest the majority are only possible for cubic close packing of the X atoms. Chains that can be accommodated in sphere packings with h layers are the *trans* chain and the *cis* chains e_2, z_6 and $(ezz)_2$ (the index number indicates the number of repeating units needed to reach a translationally equivalent position). Chain symmetry and packing requirements dictate that certain symmetry elements of the sphere packing cannot be retained; with these symmetry restrictions the possible space groups are deduced using group–subgroup relationships. For 16 chain types the most important packing possibilities are illustrated. The known structure types $NbCl_4$, α-NbI_4 and $OsCl_4$ (*trans* chain), $ZrCl_4$, $TcCl_4$ and UI_4 (*cis* chain e_2), ZrI_4 [*cis* chain $(ess)_2$] and HfI_4 [*cis* chain $(es)_2$] correspond to some of the predicted possibilities. γ-PtI_4 (*cis* chain e_2) is an exception in that the packing of its I atoms deviates considerably from close packing.

Einleitung

Unter den Verbindungen der Zusammensetzung MX_4 trifft man vor allem drei Typen von Atomverbänden an: (1) Monomere Moleküle mit Tetraederstruktur, z.B. $SiCl_4$; (2) Schichtstrukturen mit eckenverknüpften Oktaedern, z.B. SnF_4; (3) Ketten von kantenverknüpften Oktaedern. Daneben gibt es einige besondere Strukturtypen, z.B. Käfigmoleküle wie beim $(TeCl_4)_4$, Ketten von Oktaedern, die abwechselnd über Flächen und Ecken verknüpft sind, beim $ReCl_4$ oder Strukturen mit höherer Koordinationszahl als sechs für das M-Atom, z.B. beim ZrF_4 oder UCl_4.

In der vorliegenden Arbeit werden die Strukturmöglichkeiten für MX_4-Verbindungen vom vorgenannten Typ (3) behandelt. Diesen Typ trifft man vor allem bei den nicht-fluoridischen Tetrahalogeniden der schwereren Nebengruppenelemente an. Es werden die möglichen Strukturen für Ketten von kantenverknüpften Oktaedern abgeleitet und es wird eine Nomenklatur dafür vorgeschlagen. Wenn solche Ketten unter Einhaltung bestimmter Randbedingungen zu

0567-7408/81/030532-14$01.00